
BRUNO: BACKPROPAGATION RUNNING UNDERSAMPLED FOR NOVEL DEVICE OPTIMIZATION

Luca Fehlings¹, Bojian Zhang¹, Paolo Gibertini¹, Martin A. Nicholson¹, Erika Covi¹, and Fernando M. Quintana¹

¹Zernike Institute for Advanced Materials & Groningen Cognitive Systems and Materials Center (CogniGron)
University of Groningen, 9747 AG Groningen, Netherlands

January 14, 2026

ABSTRACT

Recent efforts to improve the efficiency of neuromorphic and machine learning systems have centred on developing of specialised hardware for neural networks. These systems typically feature architectures that go beyond the von Neumann model employed in general-purpose hardware such as GPUs, offering potential efficiency and performance gains. However, neural networks developed for specialised hardware must consider its specific characteristics. This requires novel training algorithms and accurate hardware models, since they cannot be abstracted as a general-purpose computing platform. In this work, we present a bottom-up approach to training neural networks for hardware-based spiking neurons and synapses, built using ferroelectric capacitors (FeCAPs) and resistive random-access memories (RRAMs), respectively. Unlike the common approach of designing hardware to fit abstract neuron or synapse models, we start with compact models of the physical device to model the computational primitives. Based on these models, we have developed a training algorithm (BRUNO) that can reliably train the networks, even when applying hardware limitations, such as stochasticity or low bit precision. We analyse and compare BRUNO with Backpropagation Through Time. We test it on different spatio-temporal datasets. First on a music prediction dataset, where a network composed of ferroelectric leaky integrate-and-fire (FeLIF) neurons is used to predict at each time step the next musical note that should be played. The second dataset consists on the classification of the Braille letters using a network composed of quantised RRAM synapses and FeLIF neurons. The performance of this network is then compared with that of networks composed of LIF neurons. Experimental results show the potential advantages of using BRUNO by reducing the time and memory required to detect spatio-temporal patterns with quantised synapses.

Keywords Learning · FeCAP · neuromorphic · SNN · RRAM

1 Introduction

The rapid growth of artificial intelligence (AI) demands efficient hardware solutions that enable energy-efficient computing without sacrificing performance. However, current AI hardware faces fundamental trade-offs between power consumption, computational efficiency, and accuracy. Furthermore, the storage and routing of synaptic weights remains one of the major challenges for efficient hardware platforms for Spiking Neural Networks (SNNs) [1]. While advantageous, quantisation of synaptic weights can introduce noise and nonlinearity that degrade the network's accuracy performance in inference. Neurons using innovative devices promise better noise rejection [2] and, as we will show, allow strict weight quantisation. Moreover, memory devices have shown potential in their application in Machine Learning (ML) and neuromorphic engineering for in-memory computing [3] due to their non-volatility, compact size, and low latency [4]. Thanks to these properties, devices such as Resistive random-access memory (RRAM), phase-change memory (PCM) or ferroelectric devices offer situational advantages over traditional memories such as static random-access memory (SRAM). Their non-volatility makes it possible to store the parameters of ML models

without a constant power supply. This characteristic makes them ideal for representing static and plastic synapses of an artificial neural network.

However, the use of these memory devices within an application-specific integrated circuits (ASICs) requires accurate physical or behavioural models. These models typically represent the network synapses, where their behavioural models are incorporated into simulation frameworks and training algorithms [5, 6, 7, 8, 9, 10] to account for device variability in the updating process. Recent research has also incorporated physical models into machine learning frameworks such as IBM Analog Hardware Acceleration Kit (AIHWKIT) [4, 11]. However, these devices can also be used as computational primitives in the neuron to enhance its behaviour by including multiple time constants [2]. When used as computational primitives, these models have to be computationally efficient and well-posed to allow efficient temporal training methods, such as backpropagation through time (BPTT) [12]. Accurate models and efficient training are particularly important when the inherent physical dynamics of the underlying hardware are to be exploited. Algorithms and hardware need to be co-developed from memory devices and circuit technology to the whole neuromorphic system.

One of the challenges of using memory devices is that they are inherently stateful and exhibit non-linear behaviour over a wide range of timescales that need to be reliably modelled. Given that typical application timescales are on the order of 100 milliseconds to seconds [13, 14, 15], integrating these models, whose simulation timescale is on the order of microseconds, with gradient-based training algorithms, such as BPTT, would lead to a significant increase in training time and memory requirements. This is because the computational graph created for automatic differentiation contains the states at every microsecond. An alternative approach would be to increase the time step, but this would lead to model instability and inaccurate results. Therefore, we propose an innovative training method that reduces the training time by around an order of magnitude and reduces the memory consumption during training over a large number of time steps. This is achieved by using two different time resolutions for the forward and the backward passes. We call this method Backpropagation Running Undersampled for Novel device Optimization (BRUNO). This training method has several advantages, namely reducing time and memory consumption compared to BPTT, allowing us to train neural networks with high temporal dynamics, and compare the behaviour of networks with these new models with standard neurons such as leaky integrate-and-fire (LIF) [16]. To validate BRUNO, a network composed of ferroelectric leaky integrate-and-fire (FeLIF) neurons and synapses based on RRAM devices is trained and compared with LIF neurons. In addition, thanks to the BRUNO algorithm, we can showcase how hardware-based models, like the FeLIF, could outperform or match recurrent neural networks when the synaptic weights are of low bit precision.

2 Materials and Methods

2.1 Ferroelectric LIF neuron

The FeLIF neuron [2], which co-integrates complementary metal-oxide semiconductor (CMOS) and ferroelectric capacitor (FeCap) technology, uses the non-linear charge-voltage relationship of the FeCap to integrate the inputs to two different state variables, the dielectric and the ferroelectric polarization. The dielectric polarization is linear with the voltage across the capacitor and would result in the behaviour of a conventional LIF neuron. However, the non-volatile ferroelectric polarization is gated by the membrane potential V_{mem} , the voltage across the capacitor, and only increases when a certain membrane potential V_c is reached. The ferroelectric polarization then accumulates until the saturation polarization P_s is reached. The FeLIF can thus be described phenomenologically by an integrate-and-fire (IF) neuron gated by a leaky integrator (LI) (Figure 1a), resulting in a neuron capable of tracking significant inputs over long time frames.

Based on the model extracted from the FeCap-CMOS neuron circuit [2], the behaviour can be described as follows. The derivative of the membrane potential is obtained by dividing all the currents flowing into the FeCap by its capacitance and the parasitic capacitance originating from the CMOS circuit:

$$\frac{dV_{\text{mem}}}{dt} = \frac{I_{\text{syn}} - I_{\text{leak}} - I_p}{C_0 + C_{\text{par}}} \quad (1)$$

similar to a LIF neuron, where V_{mem} is the membrane potential, I_{syn} is the synaptic input current, I_{leak} is the leakage current through the ferroelectric capacitor and I_p is the displacement current of the ferroelectric polarization. The ferroelectric displacement current results from the ferroelectric polarization process under an electric field and is proportional to the derivative of the polarization:

$$\frac{I_p}{A} = \frac{dP}{dt} = \frac{\text{sign}(E_{fe}) \cdot P_s - P}{\tau(E_{fe})} \quad (2)$$

where A is the area of the device, P is the ferroelectric polarization, E_{fe} is the electric field across the ferroelectric layer and P_s is the saturation polarization. τ is the time constant of the polarization and is a function of the electric

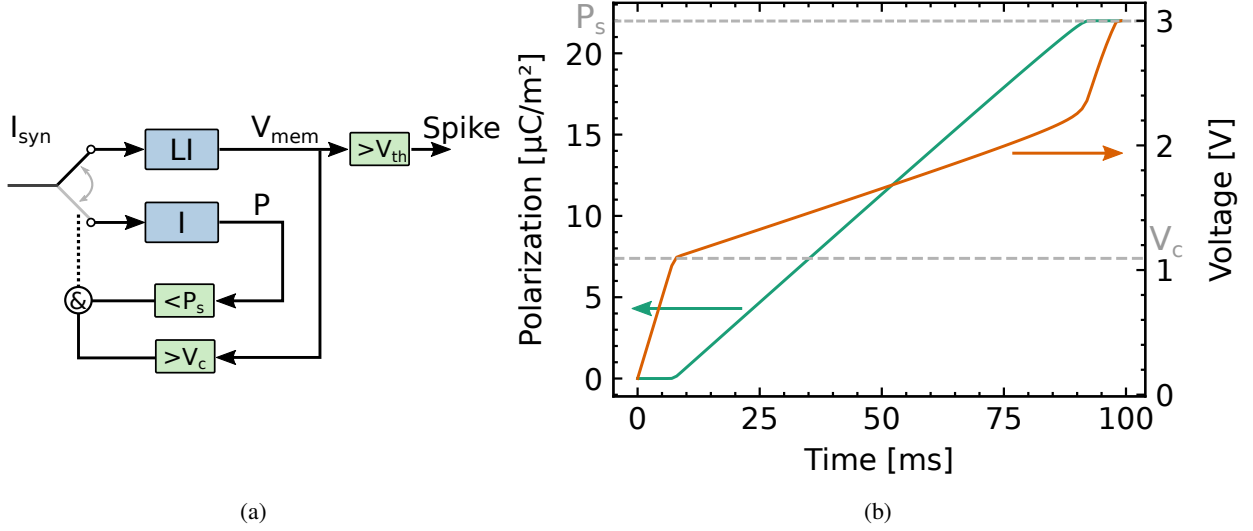


Figure 1: (a) Operating principle of the FeLIF neuron. When the membrane potential V is charged by the input current I_{syn} via the leaky integrator (LI) and reaches the coercive voltage V_c , the current partially flows to the integrator (I). When the integrator state P reaches the saturation value P_s , the current flows back to the leaky integrator until it reaches the firing threshold and the neuron emits a spike. (b) Polarization and voltage of the neuron for a constant input current. As described in the operating principle, the input current is integrated into the polarization as long as $V_{mem} > V_c$ and $P < P_s$.

Table 1: Physical parameters of the FeLIF neuron model used for simulation.

Parameter	Value
A	$25 \mu\text{m}^2$
C_0	0.558 pF
C_{par}	15 fF
P_s	$0.22 \text{ C}/\text{m}^2$
E_a	$1.27 \text{ V}/\text{nm}$
τ_0	0.1 ps
α	1.3

field:

$$\tau(E) = \tau_0 \cdot \exp\left(\frac{E_a}{|E_{fe}|}\right)^\alpha \quad (3)$$

with activation electric field E_a , elementary time constant τ_0 and the fitting factor α . The parameters described above used for the simulations are listed in Table 1.

2.2 Resistive switching non-volatile synapses

In this work, the weight quantisation is motivated by the use of RRAM as n-bit synaptic connections within the network. The RRAM switching behaviour is simulated using the Jülich Aachen Resistive Switching Tool (JART) valence change mechanism (VCM) physical compact model [17]. A detailed description of the model and the physical stack of the simulated RRAM can be found in the Supplementary Information, Section 2.1.

In this work, current-pulse programming, a common approach in neuromorphic hardware [18, 19], is used to program the RRAM device. Therefore, the analogue behaviour of the RRAM is studied with current pulses of $10 \mu\text{s}$ time width and amplitudes from $50 \mu\text{A}$ to $300 \mu\text{A}$ with $10 \mu\text{A}$ steps. After each programming pulse, a read-out operation is performed in current mode. During this read-out operation, a current pulse with $10 \mu\text{A}$ amplitude and $10 \mu\text{s}$ pulse width is applied to the RRAM and the voltage drop across the cell is measured to calculate the corresponding conductance.

Table 2: Current pulse amplitudes for 3-bits quantisation

States	Current pulse amplitude
<i>HRS</i>	10 μ A
<i>LRS</i> ₁	50 μ A
<i>LRS</i> ₂	80 μ A
<i>LRS</i> ₃	110 μ A
<i>LRS</i> ₄	140 μ A
<i>LRS</i> ₅	180 μ A
<i>LRS</i> ₆	230 μ A
<i>LRS</i> ₇	300 μ A

To qualitatively discuss the impact of RRAM stochasticity on device programming, the filament-related parameters responsible for the conductance variation are varied by 1σ from their mean values, as shown in the Supplementary Information, Table 2.

The quantised values of the RRAM were obtained with current pulses of 10μ s time width and amplitudes as in Table 2. Note that these values were obtained with partial set operations starting from the high resistive state (HRS) and reaching different intermediate low resistive states (LRS).

2.3 Quantisation-Aware training

The quantisation of the synapses throughout the training process has to be considered to adequately model the RRAM-based synapses. Weight quantisation is incorporated into the training phase using the Quantisation Aware Training (QAT) process [20]. Since the quantisation operation is non-differentiable, a surrogate quantisation operation is used to perform the weight quantisation. This means that quantisation is applied in the forward pass, but is replaced by an approximate differentiable function in the backward pass.

$$w_q = \text{sround} \left(\frac{w}{s_w} \right) \quad (4)$$

$$s_w = \frac{\max(|w|)}{2^{N-1} - 1} \quad (5)$$

The quantisation operator is defined in the equation 4, where the trained floating-point weight value w is scaled by a factor s_w defined in the equation 5, where N is the number of bits to be considered. The scaled weight is then applied to a stochastic rounding operator [21]. Since the gradient of the rounding is approximately zero over the domain, the straight-through estimators (STE) surrogate gradient is applied to it [22, 23].

3 Results

3.1 Training algorithm

Training physically accurate neuron models with different temporal dynamics can cause instabilities at simulation timescales of ≈ 1 ms. In addition, training at finer timescales of around 1μ s can increase computational resources by three orders of magnitude. BRUNO uses a dual timescale for the forward pass and the gradient computation. Figure 2 illustrates the training procedure. In the forward pass, the network simulation runs with a fine-grained simulation time step of 1μ s. However, the gradient calculation is performed with a 1 ms time step. This reduces the size of the unrolled computational graph during backpropagation by reducing the total number of time steps in the backward pass. To achieve the dual timescale training, the calculation of the internal state of the neuron can be computed on both time steps and use the higher timescale gradient as a surrogate gradient for the 1μ s time resolution value (Algorithm 1).

To validate BRUNO, the FeLIF model described in section 2.1 is used. The internal state of the neuron $s^t = \{V^t, P^t\}$ is defined as the voltage and polarization over time. The algorithm 1 shows the pseudocode of the training method. In the forward pass, the value of the neuron state at time t (s^t) is calculated with microsecond ($s_{\mu s}$) and millisecond (s_{ms}) time resolution. By applying the function $s_{ms} + \text{detach}(s_{\mu s} - s_{ms})$, the state of the neuron is equal to $s_{\mu s}$. However, as the subtraction $s_{\mu s} - s_{ms}$ is detached from the computational graph, the gradient flows throughout the millisecond time scale state (s_{ms}). The final voltage v_{mem} obtained from s_{ms} is then applied to a threshold operator

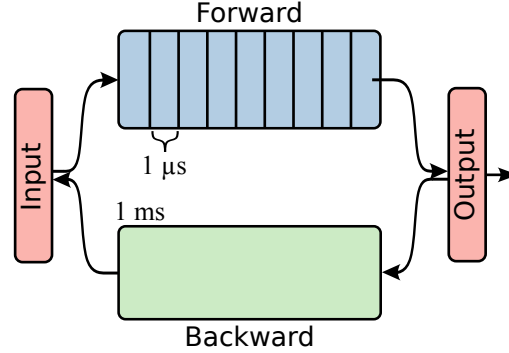


Figure 2: Schematic of the algorithm for computing the forward and backward passes with different time steps. During the forward pass (blue box) the simulation operates on $1 \mu\text{s}$ timescale. In the backward pass (green box) the gradient is calculated on 1ms timescale.

sg that applies a surrogate gradient [24]. When the neuron fires, the state is reset. The software implementation of BRUNO is publicly available on Github¹

Algorithm 1 BRUNO

```

for  $t = 1, \dots, T$  do
   $s_{\mu s}^0 \leftarrow s^{t-1}$ 
  for  $i = 1, \dots, 1000$  do
     $s_{\mu s}^i \leftarrow$  compute  $s$  based on equations 1 - 3 with  $1 \mu\text{s} \Delta t$ 
  end for
   $s_{ms} \leftarrow$  compute  $s$  based on equations 1 - 3 with  $1 \text{ms} \Delta t$ 
   $s^t \leftarrow s_{ms} + \text{detach}(s_{\mu s} - s_{ms})$ 
  spike  $\leftarrow sg(v_{mem}^t - v_{thr})$ 
  reset  $s^t$  in case of spike
end for

```

3.2 Verification and benchmarking

To verify the functionality of BRUNO on a physically accurate neuron model for future hardware deployment, first, the behaviour of the FeLIF Python model used during training is verified to match the Simulation Program with Integrated Circuit Emphasis (SPICE) simulations of the FeLIF circuit. Second, the RRAM stochasticity and quantisation for the synapse implementation are analysed. Finally, a comparison and analysis of BRUNO and BPTT is performed, examining the differences in training time and memory consumption. This is followed by benchmarking an SNN on different spatio-temporal datasets, with the results compared across different cases involving different quantisation levels for the weights and different neuron models.

3.2.1 Hardware model and verification

A comparison of the SPICE circuit simulations and the behavioural model (equations 1-3) shows a close match in the transient of the ferroelectric polarization (Figure 3a) as well as in the membrane potential of the neuron (Figure 3b). While the network simulation resets the membrane potential as soon as the firing threshold is crossed, the circuit needs to reset the physical device, resulting in an overshoot in the voltage. However, since it happens during the refractory period, it does not affect the operation of the neuron in the network simulations.

3.2.2 Synaptic Stochastic and Quantisation analysis

Due to their non-volatility and small footprint, RRAMs were chosen as the artificial synapses for the neural networks used in the BRUNO benchmarking. They operate on the principle of the formation or rupture of conductive filaments, resulting in the switching between LRS and HRS. However, due to the physical processes leading to this switching (the random formation and rupture of the conductive filaments during the SET and RESET processes [25]), RRAM

¹<https://github.com/bics-rug/ELEANOR>

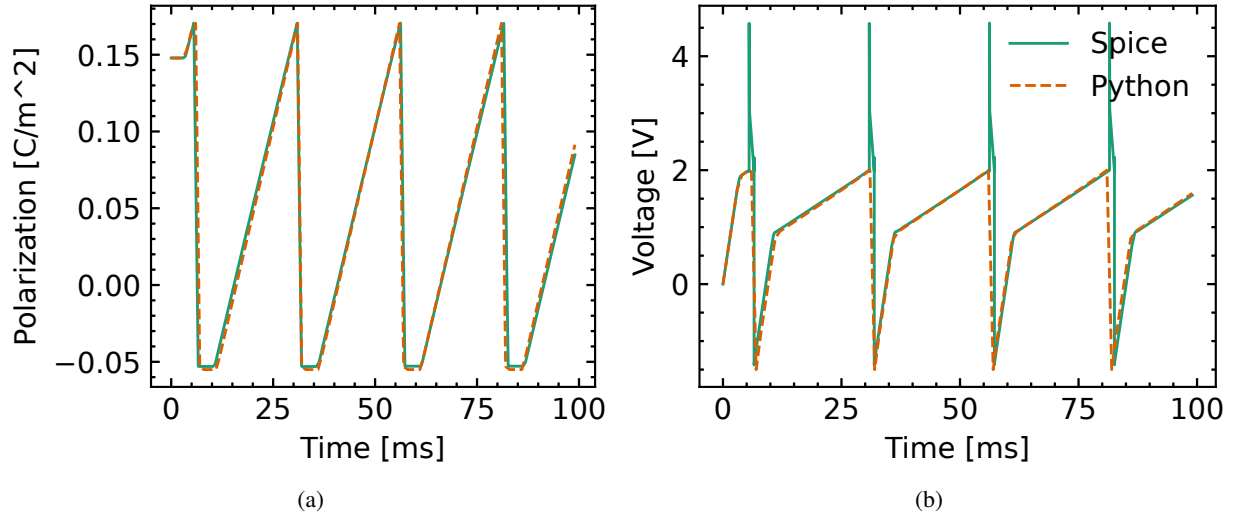


Figure 3: Comparison of the membrane potential transient between the SPICE simulation of the neuron circuit and the model used in the network simulations with a DC input current of 308 pA. Except for the spike amplitude, the polarization (a) and the voltage (b) match between the Python and SPICE simulations. The amplitude of the spike in the network is negligible as it is registered as an event in any case.

devices exhibit inherent stochasticity, leading to Cycle-to-Cycle (C2C) variability. As a result, adjacent conductance states may overlap, making them indistinguishable. Therefore, quantisation is required to define a limited number of discrete, non-overlapping conductance levels to ensure distinguishable weights/conductance states. The inherent stochastic behaviour of RRAM devices was incorporated into the device simulations using stochastic rounding as described in Section 2.3.

Before quantizing the RRAM programmed states, it is essential to investigate the RRAM analogue weight update behaviour and assess its linearity. Figure 4a illustrates the change in conductance in response to an increase in the amplitude of the programmed current pulse, as well as the maximum variability of the programmed conductance state due to the stochastic switching behaviour [26, 27]. It can be observed that a quasi-linear change in conductance follows the application of each programming pulse, with an increase in the amplitude of the current pulse. However, the C2C variability limits the number of states that can be reliably read, since the same analogue conductance state can be obtained with different current values. As a result, the distributions of different states overlap, preventing a correct reading. To reliably extract distinguishable RRAM programmed states from the quasi-analogue weight update, state quantisation is performed. Based on the data in Figure 4a, 3-bit states have been quantised. Figure 4b illustrates the distribution of 3-bit quantised states obtained from Monte Carlo (MC) simulations, which included 7 LRS states extracted from the analogue weight update curve and 1 initial HRS state, as explained in Section 2.2. The distribution of conductance within 2σ over the selected programming pulses shows a clear distribution across the entire conductance range. The distribution of adjacent conductance states shows a distinct gap with an average of 20 μ S, which is sufficient to be detected by standard CMOS circuitry.

3.2.3 Benchmark

To evaluate the performance of BRUNO on a high-temporal-resolution model such as the FeLIF neuron, two spatio-temporal datasets were used. Firstly, the Johann Sebastian Bach (JSB) music chorales dataset [28] was used for music generation, with notes represented as input spikes at each time step. Secondly, the Neuromorphic Braille Reading Dataset [29]. This consists of 5,400 Braille reading samples recorded by an Omega 3 robot with a sensorised fingertip that moves over 3D-printed Braille letters [29]. Furthermore a comparison between training with BPTT and BPTT with checkpoints (BPTT-C) or BRUNO were made on both datasets.

To BRUNO or not to BRUNO Training a neural network for long sequences ($>1M$) with BPTT can cause memory and time problems during training, as it has to store internal states for every time step. Methods like checkpointing [30] can reduce the memory consumption by storing only key states, but during the backpropagation the intermediate states that were not stored need to be recomputed. In the case of BRUNO, there is no need to recompute the intermediate states, since it backpropagate with a higher time step. (Fig. 5).

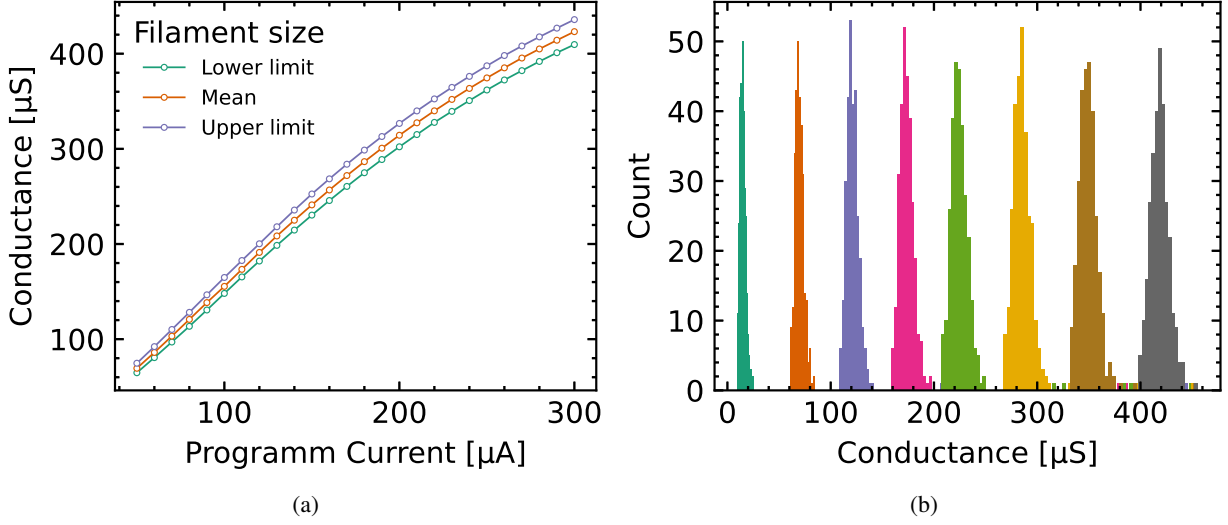


Figure 4: RRAM state programming and device conductance. (a) Device conductance based on the programming current applied, for a mean filament size of 0.4 nm length and 45 nm filament radius, an upper limit of 0.36 nm length and 49 nm filament radius, and a lower limit of 0.44 nm length and 41 nm filament radius. (b) Distribution of the different 3-bit quantised states.

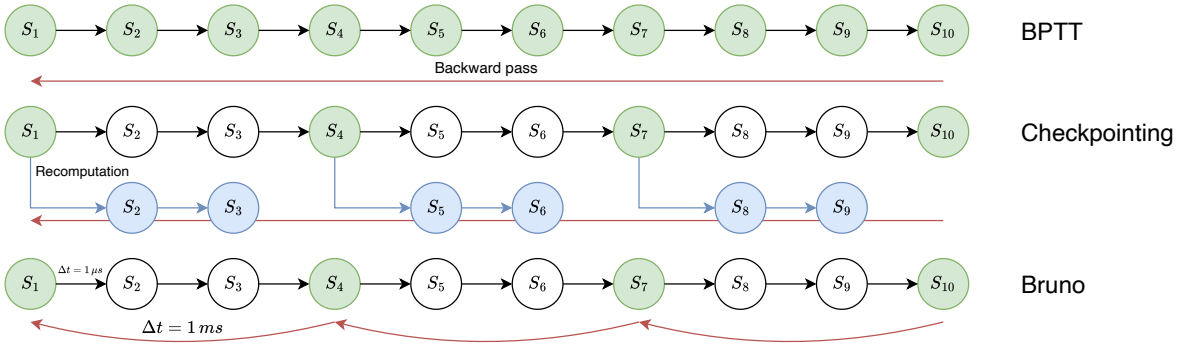


Figure 5: Comparison of forward and gradient calculations of BPTT, checkpointing and BRUNO. The green nodes represent points saved in memory and the blue nodes represent those that has be recomputed during the backward pass with checkpointing. In BPTT the internal states of the model are stored at each time step, which increases memory consumption. Checkpointing provides a trade-off between time and memory, by storing key state points; however, it must recompute the intermediate states during backpropagation, which increases computation time. In the case of BRUNO, internal states at at key times are stored for the backward pass as with checkpointing. Furthermore, gradient computation does not recompute all intermediate states, as gradient computation occurs at a different timescale. This reduces the training time and memory consumption compared to BPTT and checkpoints.

Figure 6 compares the training time and memory consumption of training a neural network with difference size (128, 256 and 512 neurons) with different sequence lengths for BPTT, BPTT-C and BRUNO. In the case of BPTT-C different number of checkpoints where used by trading memory and training time (since it need to recompute more nodes). BRUNO improves both training time and memory utilization compared to the other methods.

Although the gradient calculation with BRUNO can differ from BPTT and BPTT-C, we investigate its convergence and compare it with BPTT and BPTT-C by training a network with the JSB chorales and Braille reading datasets. The results in the braille recognition task show a similar loss evolution with respect to BPTT without a loss in performance (Fig. 7a). In the case of the JSB dataset BRUNO outperform training with BPTT with the same set of parameters.

Bach Chorales Music prediction The JSB dataset [28, 31] is a music prediction task, where the objective is to predict the next musical note based on previous inputs. A single layer network of FeLIF neurons were used, followed

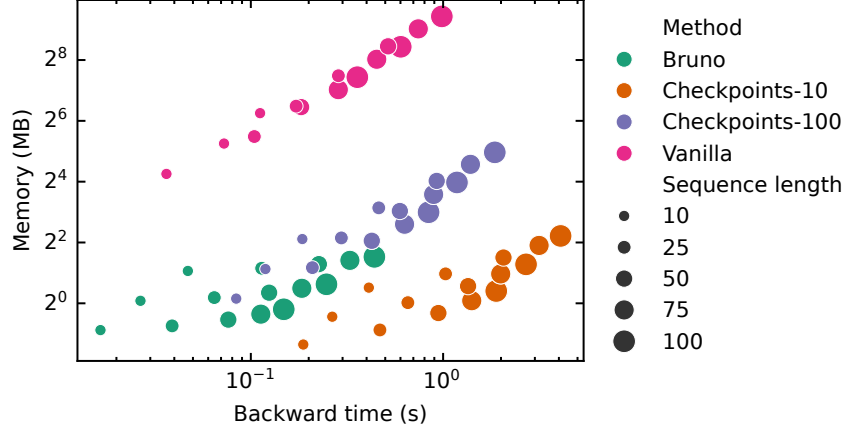


Figure 6: Memory and Time analysis between different algorithms. Each method is represented with a different color, where the size of the dots are the sequence length of input sequence. Bruno has an improvement in performance compare in the memory saving and gradient calculation time compare to method like checkpoint, that provides a tradeoff between time and memory resources.

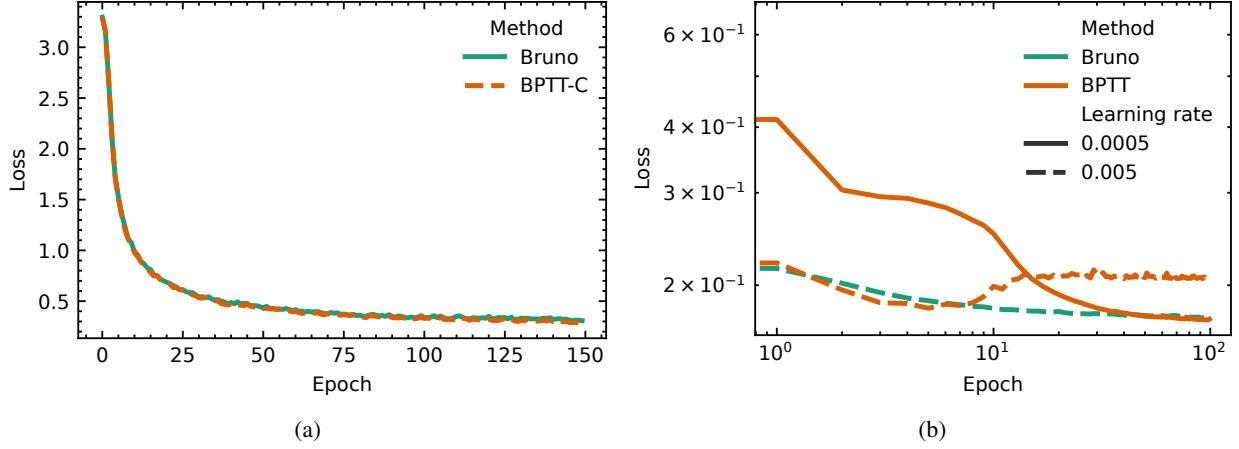


Figure 7: Comparison between training with BRUNO or BPTT/C on the JSB and Braille reading datasets. Figures a) and b) shows the loss evolution on both datasets for each method. (a) Loss between Bruno and BPTT-C on the Braille reading dataset. (b) Loss between Bruno and BPTT on the JSB dataset. In the case of BPTT multiple learning rate where used, without an improve in performance in comparison with BRUNO. All the parameters where the same for each method.

by a linear layer with sigmoid activation. The output of the network corresponds to the probability of each note to be play at each time step. The loss function used is the sigmoid cross-entropy defined at each time step.

$$L = - \sum_{c=1}^M y \log(p) \quad (6)$$

Where M is the number of notes, $y \in \{0, 1\}$ represents if the note is active, and the p is the probability that each note will be activated in each time step provided by the sigmoid activation function.

The FeLIF neuron trained with BRUNO shows good training capabilities on this datasets, surpassing a network with LIF neurons (Table 3 and Figure 8). For the network with LIF neurons, a decay of 0.4 [32] and learning rate of 0.05 were used. For the FeLIF neurons, a $I_{dsc} = 10$ pA, learning rate of 0.005 and threshold 2.0 V where used.

Braille letter recognition To evaluate the performance of the FeLIF neuron and BRUNO on this dataset, three different networks were constructed. The three networks have an input encoding layer that expands the input dimension

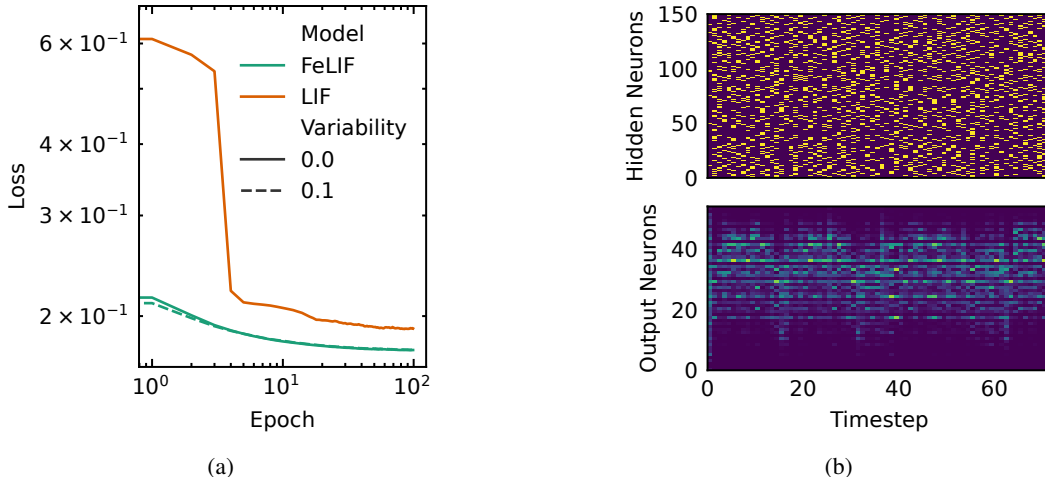


Figure 8: Comparison between training a network composed of FeLIF and LIF neurons on the JSB music prediction task. (a) Loss over 100 epochs for the JSB dataset with the FeLIF neuron model using Bruno and LIF. In the case of the FeLIF neuron, a 10% of variability on the FeCap parameters were added (Supplementary Information, Section 1.1). (b) Output spikes and probability of the network with FeLIF neurons. The upper figure represents the firing of each neuron in the hidden layer at each time step, the figure below has the output probability for each note at each time step.

Table 3: Binary crossentropy loss for different neuron models on the JSB dataset for music prediction, where the network with FeLIF neurons are trained with BRUNO.

Network	μ	σ
LIF	0.189365	3.795×10^{-3}
FeLIF	0.174426	5.54×10^{-4}
FeLIF (10% variability)	0.174613	3.37×10^{-4}

to 256, a hidden layer of 256 LIF neurons, which transforms the expanded analogue sensor values of the Braille letters into spikes. The output layer consists on 27 neurons, representing each of the Braille letters, including the space. The first network uses FeLIF neurons in the output layers (Figure 9a), while the second uses LIF neurons (Figure 9b). Moreover, for spatio-temporal data, LIF neuron networks may have difficulty learning long temporal dependencies due to the short-term dynamics [33]. Adding explicit recurrence can improve the performance on spatio-temporal data [34]. For this reason, the third network incorporates recurrent connection weights in the hidden layer (Figure 9c). A Hyperparameter Optimization (HPO) was performed to train the three network architectures SNN with different synaptic quantisation values. The final parameters used can be found in Table 4.

Quantisation and model comparison The next validation performed was the comparison between different synaptic quantisation levels and neuron models. As explained earlier, three different networks were created comparing the FeLIF neuron model with a feedforward and recurrent LIF. For each network and quantisation value, HPO was performed using the Optuna library [35]. Once the optimal hyperparameters were obtained (Table 4) for each experiment (network and quantisation), 50 simulations were performed with different initialisation values. Figure 10 and Table 5 show the final accuracy obtained. Without quantisation, the feedforward FeLIF network achieves a similar performance as the feedforward LIF network with an accuracy of $91.44\% \pm 0.73$ compared to $91.34\% \pm 0.59$ for the FeLIF. In contrast, the recurrent network has an accuracy of $95.30\% \pm 0.61$. However, as the quantisation level of the network increases, the performance of the feedforward FeLIF becomes better than that of the LIF with recurrence, obtaining $74.73\% \pm 1.37$ and $74.26\% \pm 2.48$ respectively, compared to the feedforward LIF which drops drastically in performance to $40.48\% \pm 27.84$.

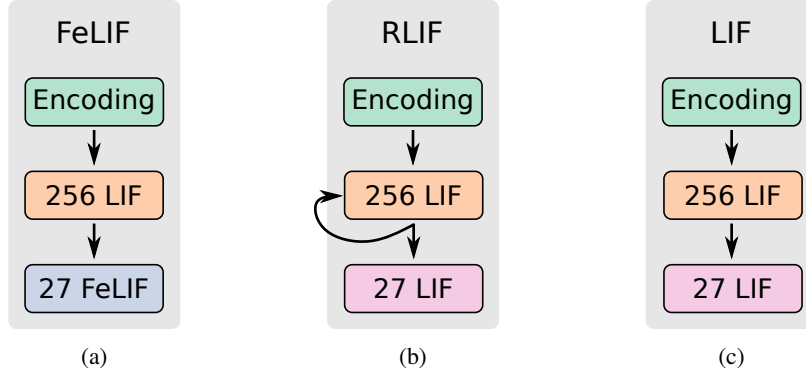


Figure 9: Network architectures used in the benchmarks. All networks contain an encoding layer, a hidden layer with 256 LIF neurons, and an output classification layer. (a) Feedforward network with FeLIF neuron in the output layer. (b) Feedforward network with the LIF neurons in the output layer. (c) Network where the LIF hidden layer has an explicit recurrent connection and the output neurons are LIF neurons.

Table 4: Parameters used for network simulations with different quantisation levels and models. The $\alpha_{hid/out}$ parameter is the membrane decay constant for the hidden and output layers. The $\beta_{hid/out}$ parameters are the synapse decay constants for the hidden and output layers. The FeLIF V_{thr} parameter is the firing threshold of the FeLIF neuron.

Quant.	Model	α_{hid}	β_{hid}	α_{out}	β_{out}	LR ¹	FeLIF V_{thr}
3	LIF	0.662	0.703	0.565	0.696	3.429×10^{-2}	-
	RLIF	0.603	0.310	0.354	0.295	1.478×10^{-3}	-
	FeLIF	0.468	0.735	-	-	7.840×10^{-4}	3.039
4	LIF	0.226	0.245	0.865	0.834	3.276×10^{-3}	-
	RLIF	0.599	0.710	0.390	0.349	6.055×10^{-3}	-
	FeLIF	0.456	0.322	-	-	3.716×10^{-3}	2.544
8	LIF	0.230	0.302	0.901	0.591	1.283×10^{-2}	-
	RLIF	0.186	0.537	0.347	0.846	6.766×10^{-3}	-
	FeLIF	0.682	0.662	-	-	4.387×10^{-3}	2.928
FP	LIF	0.959	0.202	0.716	0.600	3.006×10^{-3}	-
	RLIF	0.343	0.406	0.764	0.874	6.174×10^{-3}	-
	FeLIF	0.299	0.147	-	-	2.628×10^{-3}	3.388

¹ Learning rate

4 Discussion and conclusion

This work presents a method for training non-linear, high-temporal neuron models derived from the physical mechanisms and behaviour of analogue hardware. Due to the physics-based nature, the simulation of these models can exhibit instability when matching application time steps of ≈ 1 ms. The proposed training method is comparable to standard techniques, such as BPTT, in the training of the FeLIF model, thereby reducing the training time and memory consumption. The FeLIF neuron model was used to validate the training algorithm. The model was trained with and without BRUNO on the JSB dataset for music prediction and the Braille reading dataset, both datasets used for

Table 5: Test accuracy obtained for different quantisation levels and network architectures on the neuromorphic Braille letter reading dataset.

Network	FP32		8 bits		4 bits		3 bits	
	μ	σ	μ	σ	μ	σ	μ	σ
LIF	91.44	0.73	91.81	0.73	78.10	1.85	40.48	27.84
RLIF	95.30	0.61	95.29	0.59	91.96	0.84	74.26	2.48
FeLIF	91.34	0.59	90.69	0.57	84.49	1.22	74.73	1.37

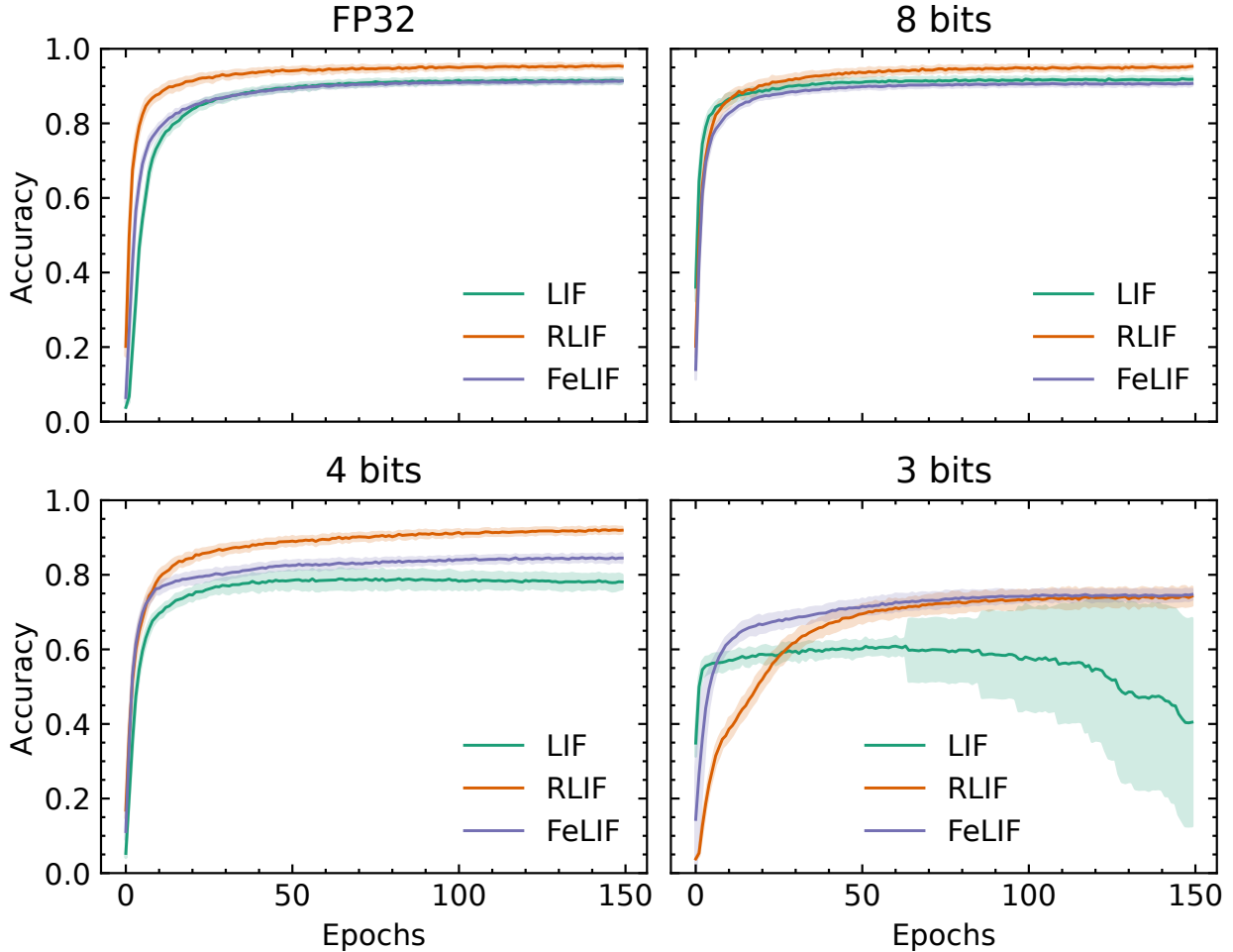


Figure 10: Accuracy on the Braille dataset with different quantisation levels and networks. Each plot has different quantisation levels (Floating-point, 8, 4, and 3 bits). In each plot, the three different network architectures are shown, trained with different initialisation seeds using the hyperparameters obtained using HPO

benchmarking spatio-temporal patterns. The results show that training with BRUNO improves training time, memory requirements, and accuracy. Achieving a reduction between 97-99% of the peak memory usage and 50-60% for reduction in training time, compared to BPTT. With an accuracy of $91.34\% \pm 0.59$ on the braille dataset. By contrast, training with BPTT-C involves a trade-off in terms of computational cost, with increased training time and reduced memory usage.

Benchmarking with feedforward and recurrent LIF networks was performed in addition to the validation of the training procedure with BPTT and BPTT-C methods. This benchmark was also performed with synaptic quantisation for its possible future implementation on hardware with RRAM synapses. Different quantisation levels were performed, for 8, 4, and 3 bits, where Hyperparameter Optimization (HPO) was performed to obtain the optimal set of hyperparameters for each network and quantisation level. As a result of this benchmark, we show that a feedforward FeLIF network has comparable results to a feedforward LIF network with $91.34\% \pm 0.59$ and $91.44\% \pm 0.73$ respectively. However, for the quantisation network, the FeLIF outperforms the feedforward LIF network and has similar performance with a recurrent LIF network with 3-bit quantisation with $74.73\% \pm 1.37$ and $74.23\% \pm 2.48$ respectively. In contrast, the mean accuracy obtained for the feedforward network is $40.48\% \pm 27.84$, which could be due to a high learning rate for the quantised weights, since the network started to lose performance drastically on the last epochs.

Thanks to the reduction in resources need for training compared to methods like BPTT or BPTT-C, BRUNO opens up the possibility of simulating and training neural models with complex dynamics that can be used for spatio-temporal pattern recognition. These neural models have the potential to be integrated into hardware with synaptic quantisa-

tion, which could provide performance comparable to that of a recurrent LIF network, while not requiring additional recurrent connections, and thus fewer trainable parameters.

Acknowledgements

We thank Pedro F. Ortiz Costa and Dr. Francesco Malandrino, Jun. Prof. David Kappel for their support and fruitful discussions. We thank the Center for Information Technology of the University of Groningen for their support and for providing access to the Hábrók high performance computing cluster. This work was partially supported by the European Union and the European Research Council (ERC) through the European’s Union Horizon Europe Research and Innovation Programme under Grant Agreements No 101042585 and 101207193. Views and opinions expressed are however those of the authors only and do not necessarily reflect those of the European Union, the European Research Council or the European Research Executive Agency. Neither the European Union nor the granting authority can be held responsible for them. The authors would like to acknowledge the financial support of the CogniGron research center and the Ubbo Emmius Funds (Univ. of Groningen).

References

- [1] Y. Yan, T. C. Stewart, X. Choo, B. Vogginger, J. Partzsch, S. Höppner, F. Kelber, C. Eliasmith, S. Furber, and C. Mayr, “Low-power low-latency keyword spotting and adaptive control with a spinnaker 2 prototype and comparison with loihi,” *arXiv preprint arXiv:2009.08921*, 2020.
- [2] P. Gibertini, L. Fehlings, T. Mikolajick, E. Chicca, D. Kappel, and E. Covi, “Coincidence detection with an analog spiking neuron exploiting ferroelectric polarization,” in *2024 IEEE International Symposium on Circuits and Systems (ISCAS)*, pp. 1–5, 2024.
- [3] D. Ielmini and H.-S. P. Wong, “In-memory computing with resistive switching devices,” *Nature electronics*, vol. 1, no. 6, pp. 333–343, 2018.
- [4] Z. Yu, S. Menzel, J. P. Strachan, and E. Neftci, “Integration of physics-derived memristor models with machine learning frameworks,” in *2022 56th Asilomar Conference on Signals, Systems, and Computers*, pp. 1142–1146, 2022.
- [5] T. Gokmen and W. Haensch, “Algorithm for training neural networks on resistive device arrays,” *Frontiers in neuroscience*, vol. 14, p. 103, 2020.
- [6] Y. Demirag, R. Dittmann, G. Indiveri, and E. O. Neftci, “Overcoming phase-change material non-idealities by meta-learning for adaptation on the edge,” *Proceedings of Neuromorphic Materials, Devices, Circuits and Systems (NeuMatDeCaS)*, 2023.
- [7] K. C. Raghunathan, Y. Demirag, E. Neftci, and M. Payvand, “Hardware-aware few-shot learning on a memristor-based small-world architecture,” in *2024 Neuro Inspired Computational Elements Conference (NICE)*, pp. 1–8, 2024.
- [8] Y. Demirag, C. Frenkel, M. Payvand, and G. Indiveri, “Online training of spiking recurrent neural networks with phase-change memory synapses,” *arXiv preprint arXiv:2108.01804*, 2021.
- [9] Z. Yu, N. Leroux, and E. Neftci, “Training-to-learn with memristive devices,” in *2022 International Electron Devices Meeting (IEDM)*, pp. 21.1.1–21.1.4, 2022.
- [10] W. Zhang, Y. Wang, X. Ji, Y. Wu, and R. Zhao, “Roa: A rapid learning scheme for in-situ memristor networks,” *Frontiers in Artificial Intelligence*, vol. 4, 2021.
- [11] M. J. Rasch, D. Moreda, T. Gokmen, M. Le Gallo, F. Carta, C. Goldberg, K. El Maghraoui, A. Sebastian, and V. Narayanan, “A flexible and fast pytorch toolkit for simulating training and inference on analog crossbar arrays,” in *2021 IEEE 3rd International Conference on Artificial Intelligence Circuits and Systems (AICAS)*, pp. 1–4, 2021.
- [12] E. O. Neftci, H. Mostafa, and F. Zenke, “Surrogate gradient learning in spiking neural networks: Bringing the power of gradient-based optimization to spiking neural networks,” *IEEE Signal Processing Magazine*, vol. 36, no. 6, pp. 51–63, 2019.
- [13] B. Cramer, Y. Stradmann, J. Schemmel, and F. Zenke, “The heidelberg spiking data sets for the systematic evaluation of spiking neural networks,” *IEEE Transactions on Neural Networks and Learning Systems*, vol. 33, no. 7, pp. 2744–2757, 2022.
- [14] H. H. See, B. Lim, S. Li, H. Yao, W. Cheng, H. Soh, and B. C. Tee, “St-mnist—the spiking tactile mnist neuro-morphic dataset,” *arXiv preprint arXiv:2005.04319*, 2020.

- [15] E. Donati, M. Payvand, N. Risi, R. Krause, and G. Indiveri, “Discrimination of emg signals using a neuromorphic implementation of a spiking neural network,” *IEEE Transactions on Biomedical Circuits and Systems*, vol. 13, no. 5, pp. 795–803, 2019.
- [16] W. Gerstner and W. M. Kistler, *Spiking neuron models: Single neurons, populations, plasticity*. Cambridge university press, 2002.
- [17] C. Bengel, D. K. Zhang, R. Waser, and S. Menzel, “Jart vcm v1 verilog-a compact model,” 2022.
- [18] P. Livi and G. Indiveri, “A current-mode conductance-based silicon neuron for address-event neuromorphic systems,” in *2009 IEEE international symposium on circuits and systems*, pp. 2898–2901, IEEE, 2009.
- [19] G. Indiveri, B. Linares-Barranco, T. J. Hamilton, A. v. Schaik, R. Etienne-Cummings, T. Delbruck, S.-C. Liu, P. Dudek, P. Häfliger, S. Renaud, *et al.*, “Neuromorphic silicon neuron circuits,” *Frontiers in neuroscience*, vol. 5, p. 73, 2011.
- [20] I. Hubara, M. Courbariaux, D. Soudry, R. El-Yaniv, and Y. Bengio, “Quantized neural networks: Training neural networks with low precision weights and activations,” *Journal of Machine Learning Research*, vol. 18, no. 187, pp. 1–30, 2018.
- [21] M. Croci, M. Fasi, N. J. Higham, T. Mary, and M. Mikaitis, “Stochastic rounding: implementation, error analysis and applications,” *Royal Society Open Science*, vol. 9, no. 3, p. 211631, 2022.
- [22] Y. Bengio, “Estimating or propagating gradients through stochastic neurons,” *arXiv preprint arXiv:1305.2982*, 2013.
- [23] Y. Zhang, Z. Zhang, and L. Lew, “Pokebnn: A binary pursuit of lightweight accuracy,” in *Proceedings of the IEEE/CVF Conference on Computer Vision and Pattern Recognition (CVPR)*, pp. 12475–12485, June 2022.
- [24] F. Zenke and T. P. Vogels, “The remarkable robustness of surrogate gradient learning for instilling complex function in spiking neural networks,” *Neural Computation*, vol. 33, no. 4, pp. 899–925, 2021.
- [25] D. Ielmini, “Resistive switching memories based on metal oxides: mechanisms, reliability and scaling,” *Semiconductor Science and Technology*, vol. 31, no. 6, p. 063002, 2016.
- [26] F. Nardi, S. Larentis, S. Balatti, D. C. Gilmer, and D. Ielmini, “Resistive switching by voltage-driven ion migration in bipolar rram—part i: Experimental study,” *IEEE Transactions on Electron Devices*, vol. 59, no. 9, pp. 2461–2467, 2012.
- [27] S. Ambrogio, S. Balatti, A. Cubeta, A. Calderoni, N. Ramaswamy, and D. Ielmini, “Statistical fluctuations in hfo x resistive-switching memory: part i-set/reset variability,” *IEEE Transactions on electron devices*, vol. 61, no. 8, pp. 2912–2919, 2014.
- [28] N. Boulanger-Lewandowski, Y. Bengio, and P. Vincent, “Modeling temporal dependencies in high-dimensional sequences: Application to polyphonic music generation and transcription,” *arXiv preprint arXiv:1206.6392*, 2012.
- [29] S. F. Müller-Cleve, V. Fra, L. Khacef, A. Pequeño-Zurro, D. Klepatsch, E. Forno, D. G. Ivanovich, S. Rastogi, G. Urgese, F. Zenke, *et al.*, “Braille letter reading: A benchmark for spatio-temporal pattern recognition on neuromorphic hardware,” *Frontiers in Neuroscience*, vol. 16, p. 951164, 2022.
- [30] W. Bencheikh, J. Finkbeiner, and E. Neftci, “Optimal gradient checkpointing for sparse and recurrent architectures using off-chip memory,” *arXiv preprint arXiv:2412.11810*, 2024.
- [31] T. Bohnstingl, S. Woźniak, A. Pantazi, and E. Eleftheriou, “Online spatio-temporal learning in deep neural networks,” *IEEE Transactions on Neural Networks and Learning Systems*, vol. 34, no. 11, pp. 8894–8908, 2022.
- [32] T. Ortner, L. Pes, J. Gentinetta, C. Frenkel, and A. Pantazi, “Online spatio-temporal learning with target projection,” in *2023 IEEE 5th International Conference on Artificial Intelligence Circuits and Systems (AICAS)*, pp. 1–5, 2023.
- [33] C. Frenkel and G. Indiveri, “Reckon: A 28nm sub-mm² task-agnostic spiking recurrent neural network processor enabling on-chip learning over second-long timescales,” in *2022 IEEE International Solid-State Circuits Conference (ISSCC)*, vol. 65, pp. 1–3, 2022.
- [34] F. M. Quintana, F. Perez-Peña, P. L. Galindo, E. O. Neftci, E. Chicca, and L. Khacef, “Etlp: Event-based three-factor local plasticity for online learning with neuromorphic hardware,” *Neuromorphic Computing and Engineering*, vol. 4, no. 3, p. 034006, 2024.
- [35] T. Akiba, S. Sano, T. Yanase, T. Ohta, and M. Koyama, “Optuna: A next-generation hyperparameter optimization framework,” in *Proceedings of the 25th ACM SIGKDD International Conference on Knowledge Discovery and Data Mining*, 2019.

Supplemental Material for: “Bruno:
Backpropagation Running Undersampled for
Novel device Optimization”

1 Ferroelectric Leaky Integrate-and-Fire (FeLIF)

1.1 Variability

To capture the variability of the hardware and the mismatch between individual neurons within the network, our model includes variability in a selection of parameters. The mean and standard deviations of the chosen parameters are shown in Table 1. As mismatch and variability depend heavily on the fabrication process and technology readiness level, we have chosen abstract values that are, however, motivated by device physics. These values are used to model performance ranging from lab-scale devices to eventual commercial applications with well-controlled fabrication processes.

Parameter	μ	σ
A	$25 \mu\text{m}^2$	$2.5 \mu\text{m}^2$
t_{hzo}	10 nm	1 nm
t_{int}	1 nm	0.1 nm
E_a	1.27 GV/m	127 MV/m
P_s	$220 \text{mC}/\text{m}^2$	$22 \text{mC}/\text{m}^2$
I_0	$100 \mu\text{A}/\text{m}^2$	$10 \mu\text{A}/\text{m}^2$

Table 1: Variability considered for all parameters

2 Resistive switching non-volatile device

2.1 Resistive switching mechanism

Memristive devices based on resistive switching Resistive Random Access Memory (RRAM), due to their capacity to support non-volatile storage of synaptic

weight, have been selected for use as artificial synapses in Backpropagation Running Undersampled for Novel device Optimization (BRUNO). In particular, this work employs the Valence Change Mechanism (VCM) as the primary switching mechanism for RRAM devices. The formation or dissolution of the conductive filament can be achieved by moving the oxygen vacancies, which are usually generated by oxygen exchange at the electrode during the forming process, back and forth in the region between the filament tip and the Bottom Electrode (BE) (or "disc" region) by switching the electric field between the Top Electrode (TE) and the BE as shown in Figure 1. These operations are designed as 'SET' and 'RESET', respectively. Consequently, the RRAM cell switches between Low Resistive States (LRS) and High Resistive State (HRS). The switching behaviours of RRAM devices are simulated using the Jülich Aachen Resistive Switching Tool (JART) VCM physical compact model [1]. In the JART VCM model, the RRAM cell is based on a $\text{HfO}_x/\text{TiO}_x$ material system. As a set of SPICE-level physical models, this model allows us to design functional Complementary Metal-Oxide Semiconductor (CMOS)-based circuits and combine them with the RRAM model to construct our testbench in cadence.

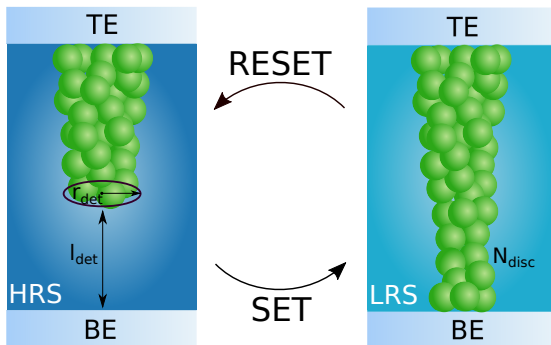


Figure 1: RRAM switching process in disc region in form of formation and dissolution of the filament caused by forward and backward moving of oxygen vacancy (represented by the green spheres) under electric field between TE and BE.

2.2 Simulation of state quantisation

State quantisation is necessary to extract the distinguishable weights, that is, the maximum number of non-overlapping states that can be confidently programmed in the proposed RRAM device when accounting for Cycle to Cycle (C2C) variability. Regarding the quantisation of the RRAM, programming currents were selected to program multiple LRS in addition to the initial HRS. Monte Carlo Monte Carlo (MC) simulations are conducted for each state, with 300 samples, to assess the impact of varying physical parameters, including maximum oxygen vacancy concentration in the disc ($N_{disc,max}$), minimum oxy-

Table 2: Variability considered for filament-related parameters

Parameter	Mean value	σ
$N_{disc,max}$	$20 \times 10^{26}/m^3$	$2 \times 10^{26}/m^3$
$N_{disc,min}$	$0.008 \times 10^{26}/m^3$	$0.004 \times 10^{26}/m^3$
r_{det}	45 nm	4 nm
l_{det}	0.4 nm	0.04 nm

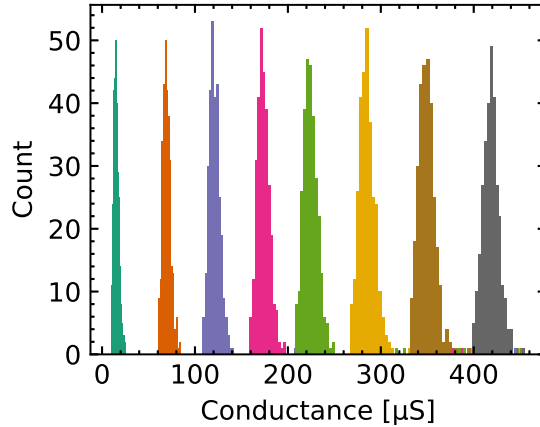


Figure 2: RRAM quantisation figure.

gen vacancy concentration in the disc ($N_{disc,min}$), length of the disc (l_{det}) and radius of filament (r_{det}). The values of $N_{disc,max}$, $N_{disc,min}$, l_{det} , r_{det} in each MC sample are selected from their respective Gaussian distributions to ensure that the quantities remain within reasonable ranges. The utilized values are listed in Table 2.

As shown in Fig. 2, for each ‘SET’ pulse amplitude, there is still a limited number of cycles that exhibit higher programmed conductance values, forming a tail of the distribution (3σ). The reason for this tail in the distribution could be related to the simulation setup. Since all the parameters related to the physical filament are randomly selected from a Gaussian distribution, it is highly likely that the combination of selected $N_{disc,max}$, l_{det} and r_{det} leads to a higher concentration of oxygen vacancies in the disc region during the ‘SET’ process, resulting in these higher conductance states. Additionally, a narrower the initial HRS state distribution can be observed in Figure 2. This narrower distribution is attributed to the initial filament physical parameter set up and the small current pulse to the RRAM cell. Firstly, the initial values of l_{det} , r_{det} converge in a narrower Gaussian distribution. Secondly, the current pulse amplitude applied to the TE in this case is 10 μ A, which is too small to trigger the ‘SET’ event. As a result, the extracted conductance value is close to the initial HRS.

References

- [1] C. Bengel, D. K. Zhang, R. Waser, and S. Menzel, “Jart vcm v1 verilog-a compact model,” 2022.